JZUS A

Effect of bedding direction of oval particles on the behavior of dense granular assemblies under simple shear[*]

Dan-da SHI[1], Jian-feng XUE[†‡1,2], Zhen-ying ZHAO[1], Yan-cheng YANG[1]

(*1School of Ocean Science and Engineering, Shanghai Maritime University, Shanghai 201306, China*)

(*2School of Engineering and IT, University of New South Wales, Campbell 2612, Australia*)

[†]E-mail: jianfeng.xue@adfa.edu.au

Abstract: Initial fabric anisotropy can greatly affect the shear behavior of particulate materials during shear. The bedding plane effect induced by particle orientation is one of the main fabric anisotropic factors that may affect other factors. It is hard to experimentally examine the effect of bedding direction of particles on the shear behavior of particulate materials, such as sand. A 2D discrete element method (DEM) is employed in this paper to study the influence of different orientations of oval particles on the behavior of dense assemblies under simple shear. As well as the macroscopic shear behavior, the evolution of particle orientation, contact normal, and inter-particle contact forces within the samples with different initial bedding angles during shear have been extensively examined. It was found that the initial bedding direction of the particles has great influence on the non-coaxiality between the directions of principal stress and principal strain increment. The bedding direction also affects the strength and dilatancy responses of DEM samples subjected to simple shear, and the samples with larger bedding angles exhibit higher shear strength and larger volume dilation. A modified stress-force-fabric relationship is proposed to describe the effect of particle bedding direction on the shear strength of samples, and the new equation can better describe the stress-force-fabric relationship of assemblies with initial anisotropic fabrics compared with the existing model.

Key words: Initial fabric anisotropy; Particle orientation; Simple shear; Non-coaxiality; Discrete element method (DEM)

http://dx.doi.org/10.1631/jzus.A1600689   **CLC number:** TU441

1 Introduction

Soil fabric was first introduced by Brewer (1964) to describe the spatial arrangement of solid particles and associated voids. Oda *et al.* (1985) summarized the three main sources of anisotropy: (1) geometrical arrangement of the particles (includes particle orientation and contact normal), (2) distribution of the contact forces, and (3) geometrical arrangement of the voids. Experimental evidence has shown that the initial fabric has great influence on the shear strength and deformation characteristics of granular soils subjected to monotonic or cyclic shear loading (Arthur and Menzies, 1972; Miura *et al.*, 1986; Guo, 2008; Tong *et al.*, 2014). The bedding plane effect induced by particle orientation is one of the main fabric factors leading to inherent anisotropy of granular assemblies (Oda and Nakayama, 1989). Early experimental studies on initial fabric mainly use ideal substituted materials such as metal rods or photoelastic substances (Drescher and de Jong, 1972; Oda *et al.*, 1982). Special apparatus or measuring techniques are required to investigate real sand specimens. For instance, Oda (1972) used polyester-resin to "freeze" the internal fabric of anisotropic sand

samples. Thin sand plates were cut from the specimens to observe the preferred particle orientation using an optical microscope. Alshibli *et al.* (2000) employed an X-ray computed tomography (CT) technique to disclose the internal fabric and the local deformation of dry Ottawa sand specimens subjected to drained triaxial shear loading in a microgravity environment. Ng *et al.* (2002) utilized a magnetic resonance imaging technique to capture the initial fabric of saturated dense Ottawa sand, and to obtain the void distribution. These advanced measuring techniques provide useful experimental measures to explore the geometric arrangement of particles and voids, but it is time-consuming to prepare the samples and expensive to run the tests. In addition, important information about the distribution of contact forces cannot be revealed even with the most advanced experimental methods mentioned above.

The discrete element method (DEM) has been proved to be a powerful tool to study the micro mechanics of granular materials (O'Sullivan, 2011; Yang *et al.*, 2013; Jiang *et al.*, 2015; Lai *et al.*, 2016; Shi *et al.*, 2016). The major advantage of DEM is that the wealth of micromechanical and statistical information can be easily obtained along with the macroscopic responses. To study the bedding plane effect, non-circular particles or non-circular clumped particles are normally used in 2D DEM models. Ting and Meachum (1995) used elliptical particles of different sizes to investigate the effect of bedding orientation on the biaxial shearing behavior of granular systems, showing that the samples with bedding plane normal to the major principal stress direction exhibited the highest shear resistance and the largest dilatancy. Mahmood and Iwashita (2010) studied the influence of inherent anisotropy on shear band formation within biaxial loaded granular assemblies using elliptical particles of aspect ratio (AR) 1.5. The particles were generated in DEM by overlapping five circular discs. Some of the phenomena observed in natural granular materials have been simulated in their models, such as the generation of large voids and excessive particle rotation inside the shear band, which are hard to simulate using circular particles. Yan and Zhang (2013) and Yang *et al.* (2013) used planar elliptical particles to study the effect of initial fabric on the critical state behavior of granular masses under biaxial shear. They found a unique fabric structure at the critical state regardless of initial different fabrics. Seyedi Hosseininia (2013) used irregularly polygon-shaped particles to assemble inherently anisotropic samples, and a theoretical stress-force-fabric relationship was developed to consider both inherent and stress-induced anisotropies in biaxially sheared assemblies.

To date, the reported DEM investigations on inherently anisotropic samples mostly focus on samples under biaxial shear, but little work has been done on the response of such samples under simple shear. Different from biaxial shear, the distinctive feature of simple shear is the rotation of principal stress and principal strain increment directions induced by shear. During this process, the rotation of the two directions may not coincide, which results in the non-coaxiality of the two directions. The influence of initial fabric on the non-coaxiality and the stress-force-fabric relationship induced by simple shear is critical for understanding the behavior of inherently anisotropic samples under simple shear.

In this study, simple shear tests were simulated using particle flow code in 2D (PFC2D) on inherently anisotropic samples with various bedding angles, i.e., the angle between the particle's long axis and the horizontal axis, using oval clumped particles. The main investigation was on the effect of bedding direction of particles on the macroscopic behavior of DEM samples and the non-coaxiality induced by the rotation of principal stress. The potential macro-micro relationships were explored in the context of the evolution of fabric anisotropy. Finally, a modified stress-force-fabric relationship was proposed to consider the effect of bedding orientation on the shear strength of the samples.

2 Numerical implementation

2.1 Sample preparation

Many different methods have been proposed to prepare DEM samples with various bedding angles. Yang *et al.* (2013) exerted inclined gravity forces on oval particles with pre-defined orientations to form inclined bedding planes. Mahmood and Iwashita (2010) and Yan and Zhang (2013) employed a method of trimming samples with different trimming angles from one gravity-deposited "seed" assembly to

form different bedding orientations. Ting and Meachum (1995) prepared initially anisotropic samples by directly prescribing the preferred direction of the generated elliptical particles' long axes. In this study, an approach similar to Ting and Meachum (1995)'s method was adopted. The main advantage of this method is to generate samples with identical initial porosity.

To generate the samples, a polydisperse granular assembly was first created using pure circular discs (i.e., "base" disc particles) with particle diameter d ranging from 0.15 mm to 0.20 mm within a 5 mm× 5 mm squared space enclosed by four rigid walls, as shown in Fig. 1a. The initial porosity n_0 of the sample is 0.12 with 935 pure circular particles. Secondly, oval clumped particles with aspect ratio of 1.6 were created using the CLUMP function built in PFC2D (Itasca, 2008) to replace the "base" particles. Each clumped particle is composed of one main disc and two attached discs with their circumferences tangent at the center of the main disc, as shown in Fig. 1b. The mass and volume (or area) of the transformed oval clumped particle are identical to those of the "base" disc particle. Therefore, the diameters of the main disc d_m and attached discs d_a can be easily calculated from the aspect ratio and the diameter d of the "base" disc particle.
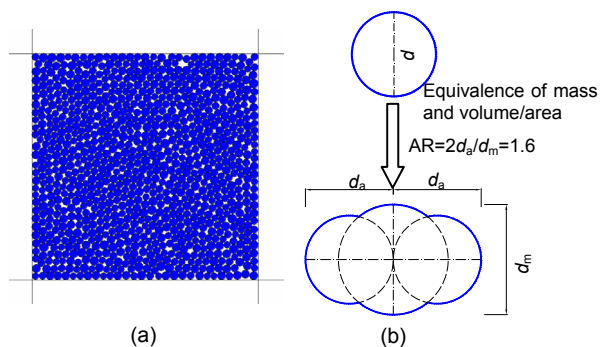

Fig. 1 Procedure of numerical sampling
(a) DEM sample with "base" disc particles; (b) Transformation from the "base" disc particle into the oval clumped particle

Five samples with bedding angles θ=0°, 30°, 45°, 60°, and 90° were generated by prescribing the long axes of the oval clumped particles along with the desired bedding angles. Then, 2000 cyclic steps were adopted in PFC2D to eliminate the possible initial overlap between the regularly arranged oval clumped particles. During this process, the initial orientation of

particles may be altered, but the major direction of the statistical distribution of particle orientation will not be significantly affected, and will be shown in the following sections. Fig. 2 shows the generated DEM samples with various bedding angles. It should be mentioned that the friction coefficients for particle-particle and particle-wall interactions are all initially set to 0 to ensure that no excessively high initial stress is created during sample preparation.
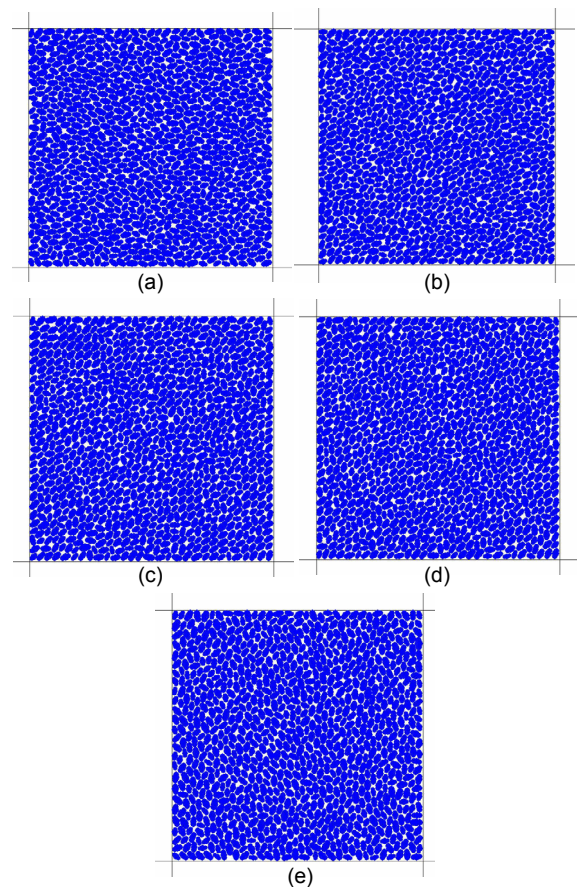

Fig. 2 DEM samples with various bedding angles
(a) θ=0°; (b) θ=30°; (c) θ=45°; (d) θ=60°; (e) θ=90°

2.2 Numerical simple shear tests

Before shearing, an isotropic confining pressure of 200 kPa was applied to the samples using the servo-control mechanism in PFC2D (Itasca, 2008). Then, as illustrated in Fig. 3a, the two lateral walls were rotated about their centroids with an angular velocity ω of 8.0×10^{-5} rad/s to shear the samples. The low shear rate is to minimize the dynamic effect between the particles. The samples were sheared at a constant vertical stress with the bottom wall fixed.

Fig. 3a shows the initial (solid lines) and final (dashed lines) positions of the walls.
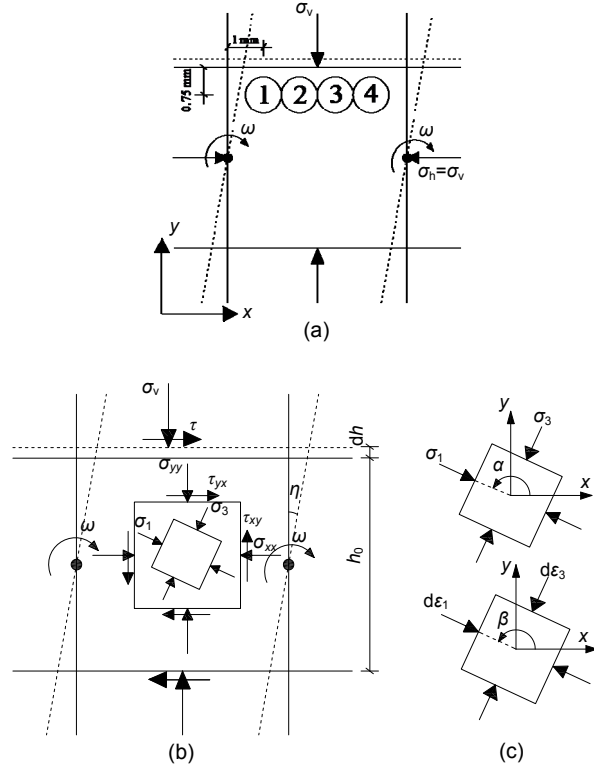

Fig. 3 Scheme for simulated simple shear tests
(a) Sample boundaries and measurement circles; (b) sample deformation and internal stress state; (c) orientations of the major principal stress α and the major principal strain increment β. σ_v or σ_h: vertical or horizontal stress; σ_{xx} or σ_{yy}: normal stress in x or y direction; τ_{xy}: shear stress ($\tau_{yx}=\tau_{xy}$); σ_1 or σ_3: major or minor principal stresses; $d\varepsilon_1$ or $d\varepsilon_3$: major or minor principal strain increment; other variables will be described in the text later

As highlighted by Cavarretta *et al.* (2010), in real granular materials, there will be damage to surface asperities and plastic yielding during the formation of particle contacts. Subsequently, significant plastic strains will develop with the increment of the stresses. In DEM, the particles are modelled with rigid particles. Munjiza (2004) described this difference as a lack of "material damping" in rigid particulate DEM codes. To avoid this, numerical damping is introduced in DEM simulations. A detailed description of the role of numerical damping in DEM analyses can be found in O'Sullivan (2011). In this study, a local non-viscous damping mechanism was used to ensure the quasi-static equilibrium of granular assemblies. To do so, damping forces are applied to the particles:

$$\boldsymbol{F}_d^p = -a\left|F^p\right|\text{sign}(\boldsymbol{v}^p), \qquad (1)$$

where $\boldsymbol{F}_d^p$ is the damping force on particle p; a is the coefficient of local damping, which is at 0.7 as recommended by Qian *et al.* (2013), Yang *et al.* (2013), and Shi *et al.* (2015); F^p is the resultant or unbalanced force acting on particle p, and $\boldsymbol{v}^p$ is the velocity vector for particle p; $\boldsymbol{F}_d^p$ is opposite to $\boldsymbol{v}^p$, and the sign($\boldsymbol{v}^p$) indicates the sign of the vector $\boldsymbol{v}^p$.

The micromechanical parameters used in the DEM simulations are summarized in Table 1. In the table, the inter-particle contact stiffness is calibrated on the basis of drained triaxial compression tests on dense Fujian standard sand (Zhou *et al.*, 2007), which is a standard sand used in China by many researchers. The inter-particle and particle and wall friction coefficient f_c was set at 0 during sample preparation and reset at 0.5 during isotropic compression and shearing, based on the reported value 0.49 by Procter and Barton (1974) for quartz sand particles. The normal and tangential contact stiffness between the walls and particles are twice those between particles to reflect the rigid wall effect.

Table 1 Micromechanical parameters for DEM simulations (Shi *et al.*, 2015)

Parameter	Value
Normal contact stiffness between particles (N/m)	2×10^8
Tangential contact stiffness between particles (N/m)	1×10^8
Coefficient of local non-viscous damping	0.7
Friction coefficient between particles	0.5
Particle density (kg/m³)	2650*
Normal contact stiffness between particle and wall (N/m)	4×10^8
Tangential contact stiffness between particle and wall (N/m)	2×10^8
Friction coefficient between particle and wall	0.5

* The particle density is 2650 kg/m³ for "base" disc particles, and when the principle of mass equivalence is adopted, the particle density for the transformed oval clumped particles is 1810 kg/m³

Fig. 3b presents the schematic diagram of simple shear deformation and the stress state of soil elements within the samples. Since there is no lateral normal strain ε_{xx} in simple shear, the shear strain γ and volumetric strain ε_v can be calculated as follow:

$$\gamma = \tan \eta, \tag{2}$$

$$\varepsilon_{\mathrm{v}} = \varepsilon_{xx} + \varepsilon_{yy} = \varepsilon_{yy} = \frac{\mathrm{d}h}{h_0}, \tag{3}$$

where η is the rotational angle of the lateral walls, and ε_{yy} is the vertical normal strain component, which is the ratio of the change of height $\mathrm{d}h$ and the initial height of the sample h_0. The volumetric strain ε_{v} is positive for contraction and negative for dilation. For convenience, the shear strain and volumetric strain are expressed in % in the paper.

The simple shear friction angle ϕ_{ss} and dilation angle ψ can be calculated by

$$\tan \phi_{\mathrm{ss}} = \frac{\tau_{xy}}{\sigma_{\mathrm{v}}}, \tag{4}$$

$$\tan \psi = -\frac{\mathrm{d}\varepsilon_{\mathrm{v}}}{\mathrm{d}\gamma}, \tag{5}$$

where τ_{xy} is the shear stress, σ_{v} is the vertical stress, and $\tau_{xy}/\sigma_{\mathrm{v}}$ is the shear stress ratio; $\mathrm{d}\varepsilon_{\mathrm{v}}$ and $\mathrm{d}\gamma$ represent the volumetric strain and shear strain increment, respectively; $-\mathrm{d}\varepsilon_{\mathrm{v}}/\mathrm{d}\gamma$ denotes the dilation ratio of the sample during shear.

As indicated by Qian *et al.* (2013), the distribution of shear stress at the top boundary in a simple shear sample is generally non-uniform. Shen *et al.* (2011) further confirmed that due to the non-uniform stress distribution at the boundaries, the shear stress ratio calculated using the boundary stress is only 80% of that calculated using the internal stresses. Therefore, the internal stresses rather than the boundary stresses were used to evaluate the shear strength of DEM samples here. To do this, four zones with a diameter of 1 mm each were assigned near the top plate to measure the internal stress and strain increment, as shown in Fig. 3a. The average values of stress components (τ_{xy}, σ_{xx}, σ_{yy}) and strain increment components ($\mathrm{d}\varepsilon_{xy}$, $\mathrm{d}\varepsilon_{xx}$, $\mathrm{d}\varepsilon_{yy}$) within the zones were used to derive the geomechanical properties of the sample. The distribution of the stresses within the samples is further discussed in Section 3.1.

As shown in Fig. 3c, the rotation of principal stress and principal strain increment directions can be captured in the simulated simple shear tests. The orientations of the major principal stress α and the major principal strain increment β relative to the

horizontal direction can be expressed as

$$\alpha = \pi - \frac{1}{2}\arctan\left(\frac{2\tau_{xy}}{\sigma_{xx} - \sigma_{yy}}\right), \tag{6}$$

$$\beta = \pi - \frac{1}{2}\arctan\left(\frac{2\mathrm{d}\varepsilon_{xy}}{\mathrm{d}\varepsilon_{xx} - \mathrm{d}\varepsilon_{yy}}\right), \tag{7}$$

where anti-clockwise rotation is defined as positive for α and β.

3 Macromechanical properties

3.1 Macroscopic responses to simple shear

Fig. 4 presents the macroscopic responses of the numerical samples with different bedding angles under simple shear. It is apparent from Fig. 4 that the dense granular assemblies exhibit typical volume dilation and strain-softening shear behavior, which agrees with those of dense sands under simple shear loading reported by Pradhan *et al.* (1988) and Thay *et al.* (2013). The values of the peak shear stress ratio $(\tau_{xy}/\sigma_{\mathrm{v}})_{\mathrm{p}}$ and the peak dilation ratio $(-\mathrm{d}\varepsilon_{\mathrm{v}}/\mathrm{d}\gamma)_{\mathrm{p}}$ are shown in Fig. 4 and summarized in Table 2. In Table 2, $\gamma_{1\mathrm{p}}$ and $\gamma_{2\mathrm{p}}$ denote the shear strains for $(\tau_{xy}/\sigma_{\mathrm{v}})_{\mathrm{p}}$ and $(-\mathrm{d}\varepsilon_{\mathrm{v}}/\mathrm{d}\gamma)_{\mathrm{p}}$, respectively. It can be seen in Fig. 4a and Table 2 that the samples with different bedding angles have almost the same initial shear stiffness (i.e., the initial slope of the stress-strain curve), but different peak shear stress ratios. The peak shear stress ratio increases monotonically from 0.48 to 0.88 as the bedding direction θ increases from 0° to 90°. As shown in Fig. 4b and Table 2, the volume dilation increases with the increase of bedding direction θ, and the peak dilation ratio increases monotonically from 0.24 to 0.47 as θ increases from 0° to 90°. It can also be found in Table 2 that the shear strain level for the point of peak dilation is very close to that for the peak shear strength, regardless of the variation of bedding direction, and the findings agree quite well with the experimental behavior of sands reported by Tong *et al.* (2014). Fig. 4c compares the variation of stresses in different zones within the sample with bedding angle of 0°. It shows that the average stress in zone 1 to zone 4 is similar to that in zone 5, which is assigned in the middle of the sample with a diameter of 3 mm.

This suggests that the average stress in zone 1 to zone 4 can be used to represent the stress states in the sample. The results also show that the shear stress and normal stress ratio at the boundary is only about 80% of the values inside the sample, which supports the findings of Shen *et al.* (2011).
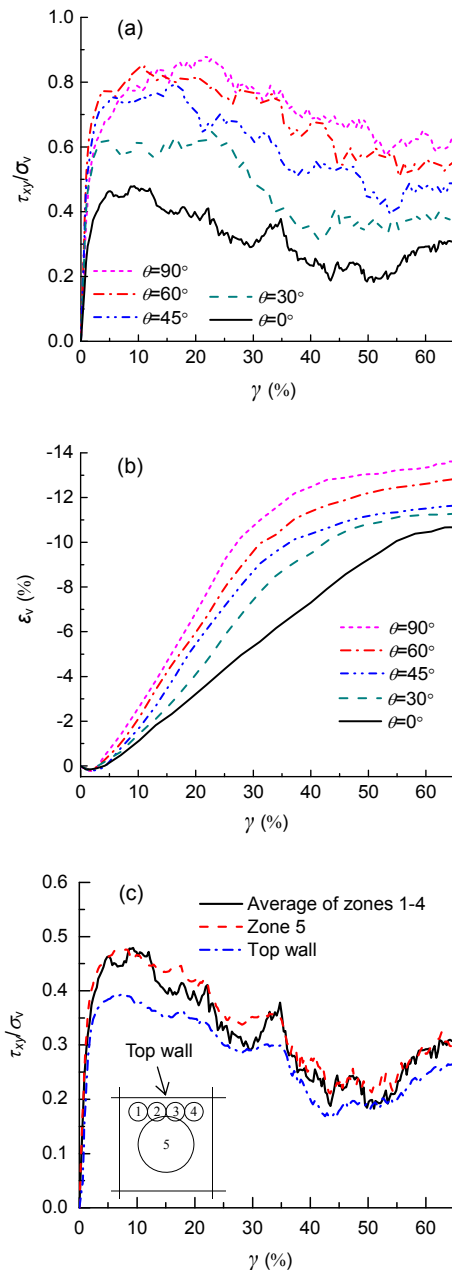
Table 2 Characteristic values of shear strength and volume dilation of DEM samples

θ	$(\tau_{xy}/\sigma_v)_p$	γ_{1p} (%)	$(-\mathrm{d}\varepsilon_v/\mathrm{d}\gamma)_p$	γ_{2p} (%)
0°	0.48	9.3	0.24	13.0
30°	0.65	22.7	0.37	25.1
45°	0.79	16.3	0.41	19.1
60°	0.85	11.2	0.44	13.0
90°	0.88	21.9	0.47	25.1

As confirmed by Shibuya *et al.* (1997) and Wang *et al.* (2007), the deformation pattern within the middle shear zone under direct shear is essentially a simple shear mode. Therefore, it can be accepted that the experimental direct shear results can be used to compare with the results of the simulated simple shear tests. The experimental results from direct shear tests on Mica sand from Tong *et al.* (2014) and quartz sand from Chen *et al.* (2014) are compared with the numerical modelling results in Fig. 5 to study the variation of the peak friction angle $(\phi_{ss})_p$ and the peak dilation angle ψ_p with the bedding angle θ. The initial porosity and vertical stress are 0.44 and 300 kPa for the direct shear tests on Mica sand (Tong *et al.*, 2014), and 0.41 and 83.3 kPa for quartz sand tests (Chen *et al.*, 2014), respectively.

Since the initial states of numerical samples and real sand samples are different, some differences have been observed in the actual values for $(\phi_{ss})_p$ and ψ_p obtained from the numerical and experimental tests, as shown in Fig. 5. The values of $(\phi_{ss})_p$ of DEM samples are smaller than those of real sands mainly owing to the differences of particle shape and surface roughness between ideal DEM particles and real irregularly-shaped sand particles (Thomas and Bray, 1999). The values of ψ_p of 2D DEM samples are greater than those of sand samples due to the fact that the volume dilations are numerically constrained within the 2D numerical model (Yang *et al.*, 2012). As discussed above, although the values of $(\phi_{ss})_p$ and ψ_p are not very consistent between numerical samples and real sand samples, the increasing tendencies of $(\phi_{ss})_p$ and ψ_p with θ are still quite comparable for 2D DEM samples and sand samples, as described in Fig. 5.

Konishi *et al.* (1983) conducted biaxial tests on samples of oval photoelastic rods, which were arranged along preferred bedding directions, and they reported that the maximum variation in the peak

Fig. 4 Macroscopic behavior of numerical samples with different θ: (a) shear stress ratio-shear strain curves; (b) volumetric strain-shear strain curves; (c) comparative curves of shear stress ratio using different measuring approaches of θ=0° sample

friction angle can be up to 8°–20° depending on the bedding plane orientation and particle angularity. In the present numerical study, as shown in Fig. 5a, the maximum increment in $(\phi_{ss})_p$ resulting from the variation of bedding angle is about 16°, which agrees with the experimental results reported by Konishi *et al.* (1983).
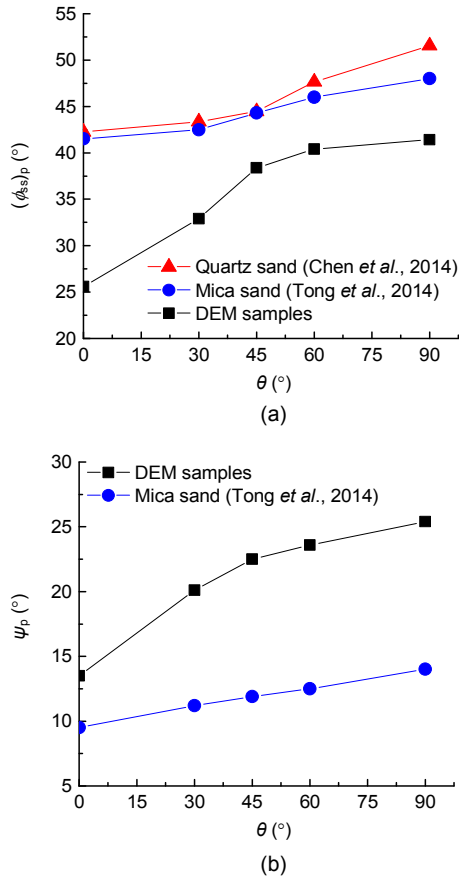

(a)

(b)

Fig. 5 Variation of the peak friction angle $(\phi_{ss})_p$ (a) and the peak dilation angle ψ_p (b) with θ (ψ_p of quartz sand was not available in Chen *et al.* (2014))

3.2 Effect of bedding angle on non-coaxiality

Shi *et al.* (2015) studied the influence of non-coaxiality on the simple shear behavior of dense granular assemblies using circular and non-circular particles with random particle orientations, but the bedding plane effect was not discussed. In this study, the influence of bedding angle θ on non-coaxiality induced by simple shear was explicitly examined. Fig. 6 shows the variation of the major principal stress

direction α and the major principal strain increment direction β with shear strain γ under various bedding directions. It can be seen that both directions rotated quickly with shear strain initially and then stabilized at the angle of 135° to the x direction at large shear strain. It is seen from Fig. 6 that for all the tested bedding angles, the major principal strain increment directions stabilized at lower strain levels, i.e., $\gamma \le 5\%$, whilst the major principal stress directions stabilized at much higher shear strain levels, i.e., up to 40%. This non-coaxiality was more obvious for the samples with larger bedding angles, which will be quantitatively discussed below.
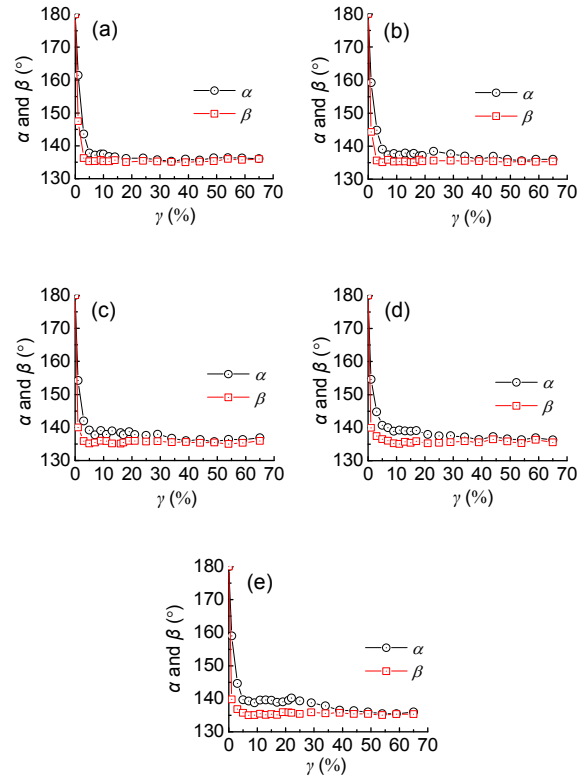

Fig. 6 Non-coaxiality between α and β during simple shear: (a) $\theta=0°$; (b) $\theta=30°$; (c) $\theta=45°$; (d) $\theta=60°$; (e) $\theta=90°$

The non-coaxiality angle Δ is introduced to quantitatively study the non-coaxility effect:

$$\Delta = |\beta - \alpha|. \tag{8}$$

Then, the non-coaxiality angle at the peak strength state (Δ_p), when ϕ_{ss} is at its peak value $(\phi_{ss})_p$, can be defined as

$$\Delta_{\mathrm{p}} = \left| \beta - \alpha \right|_{(\phi_{\mathrm{ss}})_{\mathrm{p}}} . \qquad (9)$$

Fig. 7a shows the variation of the non-coaxiality angle Δ with shear strain γ under different bedding directions. It can be seen that in general, at $\gamma \le 40\%$, the larger the bedding angle, the greater the non-coaxiality. The variation of non-coaxiality angle at the peak strength state Δ_{p} with bedding angle θ is illustrated in Fig. 7b. It shows that Δ_{p} increases monotonically from 2.2° to 4.5° as θ varies from 0° to 90°.
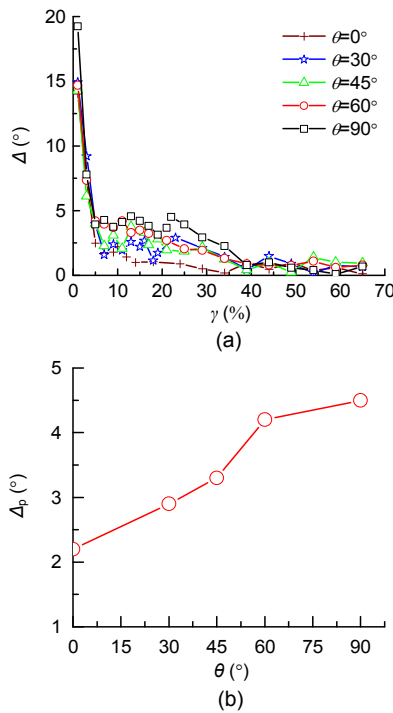
Fig. 7 Effect of the bedding angle θ on non-coaxiality
(a) Δ-γ; (b) Δ_{p}-θ

3.3 Stress-dilatancy relationship

Shi *et al.* (2015) extended the Rowe-Davis framework to study the stress-dilatancy relationship incorporating non-coaxiality:

$$\tan(\phi_{\mathrm{ss}})_{\mathrm{p}} = \frac{\tan(\phi_{\mathrm{ss}})_{\mathrm{r}} + \sin(\psi_{\mathrm{p}} - 2\Delta_{\mathrm{p}})}{\cos(\psi_{\mathrm{p}} - 2\Delta_{\mathrm{p}})}, \qquad (10)$$

where $(\phi_{\mathrm{ss}})_{\mathrm{r}}$ is the residual friction angle under simple shear.

In this section, the effectiveness of the above equation is validated using the numerical results ob-

tained earlier and some previously reported simple shear test results as shown in Table 3. It should be pointed out that in Table 3 the numerical samples with circular and angular clumped particles employed by Shi *et al.* (2015) are nearly initially isotropic, as the samples were prepared with initially random particle orientations under isotropic compression stresses. However, DEM samples introduced by Thornton and Zhang (2006) and Qian *et al.* (2013) are both initially anisotropic even though pure circular discs were used, because anisotropic compression stresses were applied before shearing. For the same reason, the samples of photoelastic rods (Oda and Konishi, 1974) and Toyoura sand (Pradhan *et al.*, 1988) also tended to be inherently anisotropic due to the process of anisotropic compression.

It can be seen from Table 3 that the non-coaxiality angle Δ_{p} of initially anisotropic samples is generally greater than that of initially isotropic ones. The calculated values of $(\phi_{\mathrm{ss}})_{\mathrm{p}}$ using Eq. (10) are very comparable to the numerical and experimental results. The differences between the predicted and measured or simulated values are mostly less than 10%. The largest difference is about −13.3%, which was observed in the numerical model on disc particles under lateral pressure coefficient K_0=2 and vertical stress of 10 MPa (Thornton and Zhang, 2006). It can be further seen from Fig. 8 that Eq. (10) well estimates the peak shear strength of dense granular assemblies when different particle shapes and initial fabrics are tested. The results show that the proposed
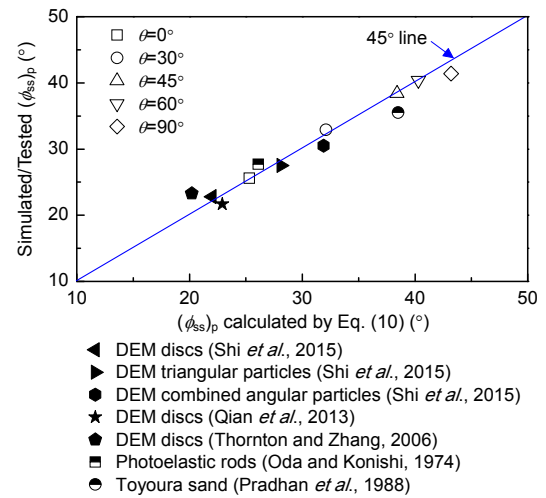

Fig. 8 Validation of the proposed stress-dilatancy relationship

Table 3 Analysis of the stress-dilatancy relationship

Sample		$(\phi_{ss})_r$ (°)	ψ_p (°)	Δ_p (°)	$(\phi_{ss})_p$ (°)		Deviation (%)
					Simulated/ Tested	Calculated by Eq. (10)	
This study	$\theta=0°$	17.2	13.5	2.2	25.6	25.3	−1.2
	$\theta=30°$	19.9	20.1	2.9	32.9	32.1	−2.4
	$\theta=45°$	26.0	22.5	3.3	38.4	38.4	0
	$\theta=60°$	29.1	23.6	4.2	40.4	40.3	−0.2
	$\theta=90°$	31.7	25.4	4.5	41.4	43.2	4.3
DEM discs (Shi *et al.*, 2015) (initially isotropic, n_0=0.12, σ_v=200 kPa)		12.4	13.2	1.5	22.8	22.0	−3.5
DEM triangular particles (Shi *et al.*, 2015) (initially isotropic, n_0=0.12, σ_v=200 kPa)		19.3	14.5	2.2	27.5	28.1	2.2
DEM combined angular particles (Shi *et al.*, 2015) (initially isotropic, n_0=0.12, σ_v=200 kPa)		20.8	18.1	2.5	30.5	31.9	4.6
DEM discs (Qian *et al.*, 2013) (initially anisotropic, n_0=0.21, σ_v=130 kPa)		20.7	7.5	2.5	21.7	22.9	5.5
DEM discs (Thornton and Zhang, 2006) (initially anisotropic, dense, σ_v=10 MPa, K_0=2.0)[*]		15.1	15.5	5.0	23.3	20.2	−13.3
Photoelastic rods (Oda and Konishi, 1974) (initially anisotropic, n_0=0.18, σ_v=130 kPa)		22.0	14.8	5.0	27.7	26.1	−5.8
Toyoura sand (Pradhan *et al.*, 1988) (initially anisotropic, n_0=0.41, σ_v=98.1 kPa, K_0=0.37)		34.7	12.6	3.5	35.5	38.5	8.5

[*] No information of initial porosity was referred in Thornton and Zhang (2006), and K_0 is the ratio of initial horizontal stress to vertical stress

stress-dilatancy relationship in Eq. (10) can effectively describe the non-coaxiality effect of granular materials under simple shear, independent of particle shape and initial fabric.

4 Evolution of fabric

4.1 Mathematical expression of fabric anisotropy

Fig. 9 schematically shows the vectors of particle orientation, contact normal, normal contact force, and tangential contact force of two contacting oval particles. To quantitatively describe the evolution of fabric anisotropy, Satake (1978) proposed the fabric tensor method, which has been used by many researchers (Oda *et al.*, 1985; Thornton, 2000; Hu *et al.*, 2010). In this method, the degree of fabric anisotropy can be easily expressed using the deviatoric fabric tensor, but the length of individual particles and the magnitude of inter-particle contact forces cannot be reflected as unit vectors are used (Yan and Zhang, 2013). Rothenburg and Bathurst (1989; 1992) proposed the Fourier approximation method to overcome the shortcoming of the fabric tensor method:
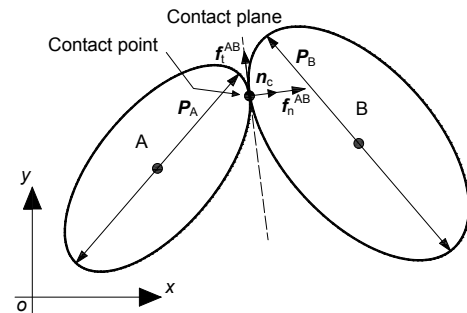
Fig. 9 Schematic diagram of two contacting oval particles
P_A, P_B: particle orientation vectors; n_c: contact normal vector; f_n^{AB}: normal contact force vector; f_t^{AB}: tangential contact force vector

$$O_p(\theta) = \frac{1}{2\pi}\left[1 + a_p \cos 2(\theta - \theta_p)\right], \quad (11a)$$

$$N_c(\theta) = \frac{1}{2\pi}\left[1 + a \cos 2(\theta - \theta_a)\right], \quad (11b)$$

$$f_n(\theta) = f_0\left[1 + a_n \cos 2(\theta - \theta_n)\right], \quad (11c)$$

$$f_t(\theta) = -f_0 a_t \sin 2(\theta - \theta_t), \quad (11d)$$

where $O_p(\theta)$, $N_c(\theta)$, $f_n(\theta)$, and $f_t(\theta)$ are the distribution functions of particle orientation, contact normal, normal contact force, and tangential contact force; a_p,

a, a_n, and a_t are the anisotropic coefficients of particle orientation, contact normal, normal contact force, and tangential contact force; θ_p, θ_a, θ_n, and θ_t are the principal direction angles of the anisotropies of particle orientation, contact normal, normal contact force, and tangential contact force, respectively; f_0 is the average value of contact normal forces over all contacts within the assembly.

4.2 Analyses of DEM samples with $\theta=0°$ and $90°$

Fig. 10 shows the deformed samples with various bedding angles at their peak strength states. Comparing with Fig. 2, the change of particle orientation induced by the shear loading can be directly seen in Fig. 10. The Fourier approximation method as described above is adopted to quantitatively study the regularities of fabric evolution. For brevity, only the fabric evolutions of the samples with $\theta=0°$ and $90°$ are discussed in this section. Figs. 11a–11c illustrate the statistical fabric distributions of the sample with $\theta=0°$ at the initial ($\gamma=0\%$), peak ($\gamma=9.3\%$), and residual ($\gamma=65\%$) states, respectively. The solid line in Fig. 11 represents the DEM statistical results and the dashed line denotes the Fourier approximation given in Eq. (11).
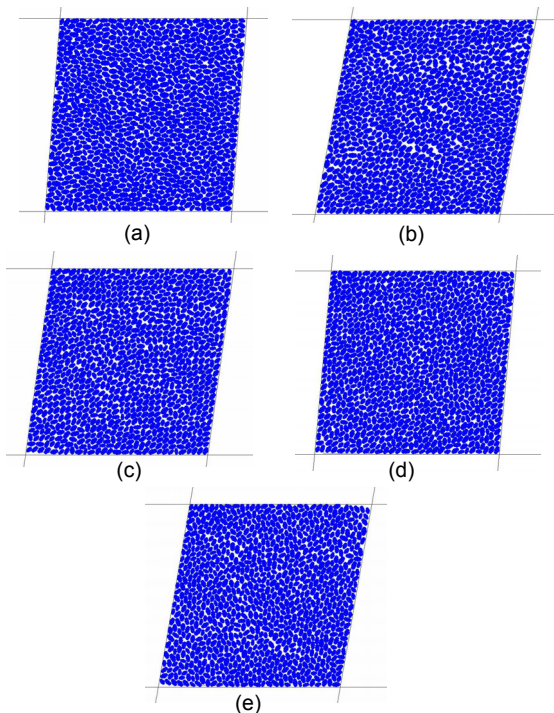

Fig. 10 Deformed samples at the peak strength states
(a) $\theta=0°$; (b) $\theta=30°$; (c) $\theta=45°$; (d) $\theta=60°$; (e) $\theta=90°$

As shown in Fig. 11a, when in the initial state, the particle orientation is mainly horizontal with θ_p at 5.5° and the main orientations of contact normal and normal contact force are near vertical (θ_a=84.3° and θ_n=83.8°) as expected. Since the samples are isotropically compressed, the tangential contact force in between the particles is minimal (Fig. 11(a4)). At the peak state shown in Fig. 11b, the major direction of particle orientation θ_p increases from 5.5° to 7.5°, with the anisotropic coefficient a_p remaining at high values. The dominant direction of contact normal θ_a changes from 84.3° to 95.5°, whilst the extent of contact normal anisotropy remains almost unchanged. The anisotropic coefficients of normal (a_n) and tangential (a_t) contact forces at the peak state increase significantly (Figs. 11(b3) and 11(b4)). The dominant directions of normal (θ_n) and tangential (θ_t) contact forces rotate from approximately vertical directions to 125.1° and 147.4°, respectively, as induced by simple shear loading. When the residual state shown in Fig. 11c is reached, the anisotropy of particle orientation (a_p) decreases owing to the disorder of the initial arrangement of particles under large shear strain. The extent of contact force anisotropies (a_n and a_t) reduces slightly because of strain-softening shear strength behavior, whilst the main directions of contact force anisotropies (θ_n and θ_t) remain almost unchanged compared with those in the peak state.

Fig. 12a describes the variation of anisotropic coefficients (a_p, a, a_n, and a_t) of the $\theta=0°$ sample with shear strain γ. It is seen from Fig. 12a that during shear, the anisotropic coefficient of particle orientation a_p is always the greatest among the four anisotropic coefficients (a_p, a, a_n, and a_t). The value of a_p starts to decrease when $\gamma\geq25\%$. The anisotropic coefficient of contact normal a does not vary much with shear strain. The anisotropic coefficients of normal and tangent contact forces (a_n and a_t) follow a similar trend to shear strain, and a_n and a_t maximize at the peak shear strength state and decrease with shear strain, which is comparable to the relationship of shear stress ratio versus shear strain shown in Fig. 4a.

Fig. 12b depicts the variation of the principal direction angles of anisotropies (θ_p, θ_a, θ_n, and θ_t) of the $\theta=0°$ sample with shear strain γ. To analyze the potential macro-micro relationships, the variation of major principal stress direction α with γ is also
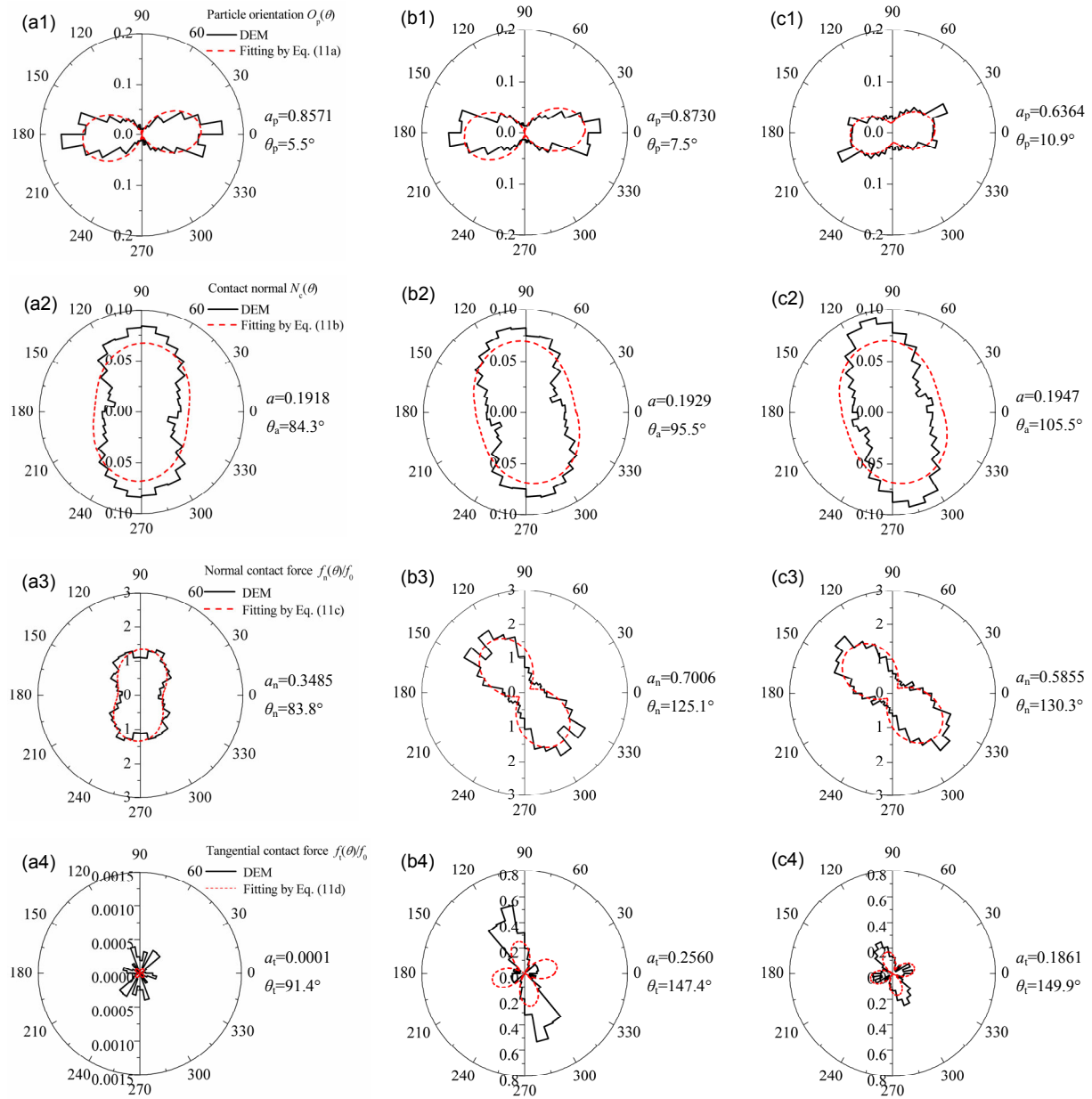
Fig. 11 Fabric evolution of *θ*=0° sample
(a) Initial state (*γ*=0%); (b) Peak state (*γ*=9.3%); (c) Residual state (*γ*=65%)
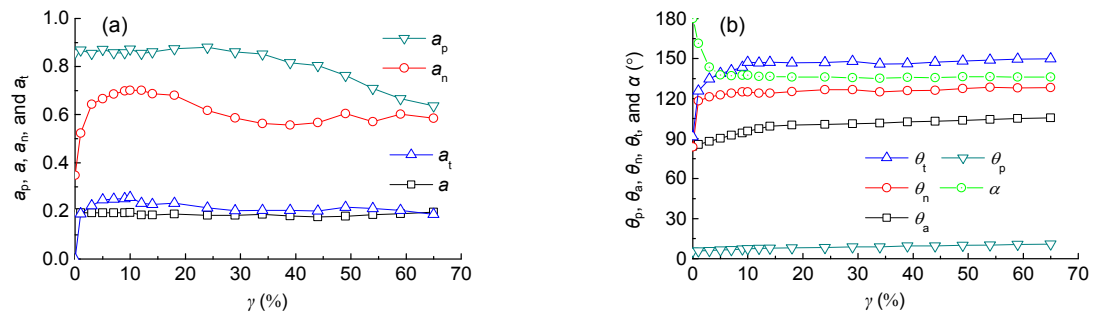

Fig. 12 Variation of anisotropic coefficients (*a*_p, *a*, *a*_n, and *a*_t) (a) and principal direction angles of anisotropies (*θ*_p, *θ*_a, *θ*_n, and *θ*_t) (b) with *γ* of *θ*=0° sample

plotted in Fig. 12b. As illustrated in Fig. 12b, the major direction of particle orientation θ_p increases slightly with γ, resulting from the rotation of the particles. During shear, the major direction of contact normal θ_a is generally perpendicular to the principal direction of particle orientation (i.e., $\theta_a \approx 90° + \theta_p$). The inclinations of principal directions of contact force anisotropies (θ_n and θ_t) rotate with the major principal stress direction α, and stabilize at the shear strain level at about 10%.

Fig. 13 shows the variation of anisotropic coefficients (a_p, a, a_n, and a_t) and the principal direction angles of anisotropies (θ_p, θ_a, θ_n, and θ_t) of the $\theta=90°$ sample with shear strain γ. It shows that the rotation of θ_a, θ_n, and θ_t and the variation of a, a_n, and a_t of the $\theta=90°$ sample follow similar trends to those of the sample with $\theta=0°$, and slightly different trends have been observed in the variation of a_p and θ_p with γ. The following section discusses the variation of the parameters with shear strain of all the samples to better explain this.

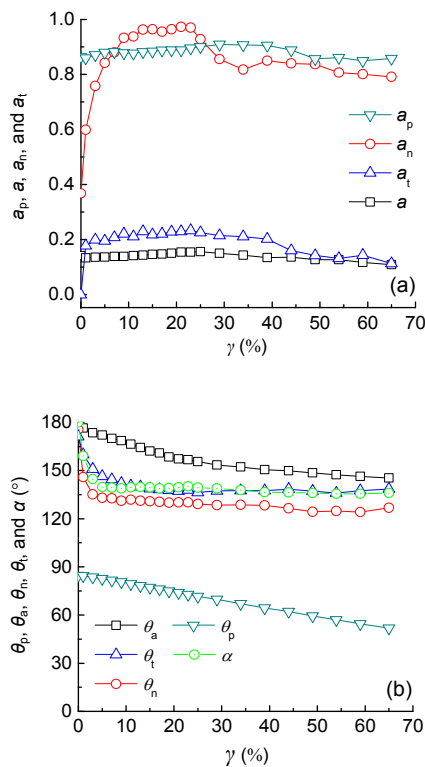**Fig. 13 Variation of anisotropic coefficients (a_p, a, a_n, and a_t) (a) and principal direction angles of anisotropies (θ_p, θ_a, θ_n, and θ_t) (b) of the $\theta=90°$ sample with shear strain γ**

4.3 Effect of bedding angle on fabric evolution

Fig. 14 shows the evolutions of anisotropic coefficients (a_p, a, a_n, and a_t) and the principal direction angles of anisotropies (θ_p, θ_a, θ_n, and θ_t) with shear strain γ of the samples with different bedding directions. It can be seen from Figs. 14(a1) and 14(a2) that a_p and a are not very sensitive to the bedding directions of the particles and do not change much with shear strain. An obvious drop of a_p has been observed in the sample with $\theta=0°$ when $\gamma \geq 25\%$. This may suggest that the initial fabric would be disorganized most easily for samples with initially horizontal bedding under simple shear loading, yet this needs to be further verified with more experimental evidence. The evolutions of a_n and a_t follow similar trends (Figs. 14(a3) and 14(a4)), which both increase with shear strain then stabilize at higher strain levels, i.e., $\gamma \geq 25\%$, but a_t is less sensitive to the bedding directions of the particles. It can also be seen that, at the same strain level, in general the higher the bedding angles the higher the a_n.

Figs. 14(b1) to 14(b4) show the variation of the principal direction angles of anisotropies (θ_p, θ_a, θ_n, and θ_t) of the samples with γ. As shown in Fig. 14(b1), the θ_p-γ curves of the $\theta=0°$ and $\theta=90°$ samples, and the $\theta=30°$ and $\theta=60°$ samples are almost symmetric to the curve of $\theta=45°$. It shows that there is a tendency of convergence of the curves towards the $\theta=45°$ curve. This is due to the fact that the directions of the major principal stress α for the samples with different bedding directions all converge to 135° at the stable state as shown in Fig. 6, namely, the directions of the major principal stress plane all converging to 45°. It further states that the major directions of particle orientation have a tendency to approach the directions of major principal stress plane under simple shear loading. During shear, as depicted in Fig. 14(b2), the major directions of contact normal are all nearly normal to the principal directions of particle orientation, irrespective of bedding angles. As Figs. 14(b3) and 14(b4) show, unlike the major directions of particle orientation and contact normal, the directions of the normal and tangential contact forces converge quickly at lower shear strain levels, i.e., $\gamma \leq 10\%$, and the directions in the residual state are not much affected by the bedding directions of the particles.
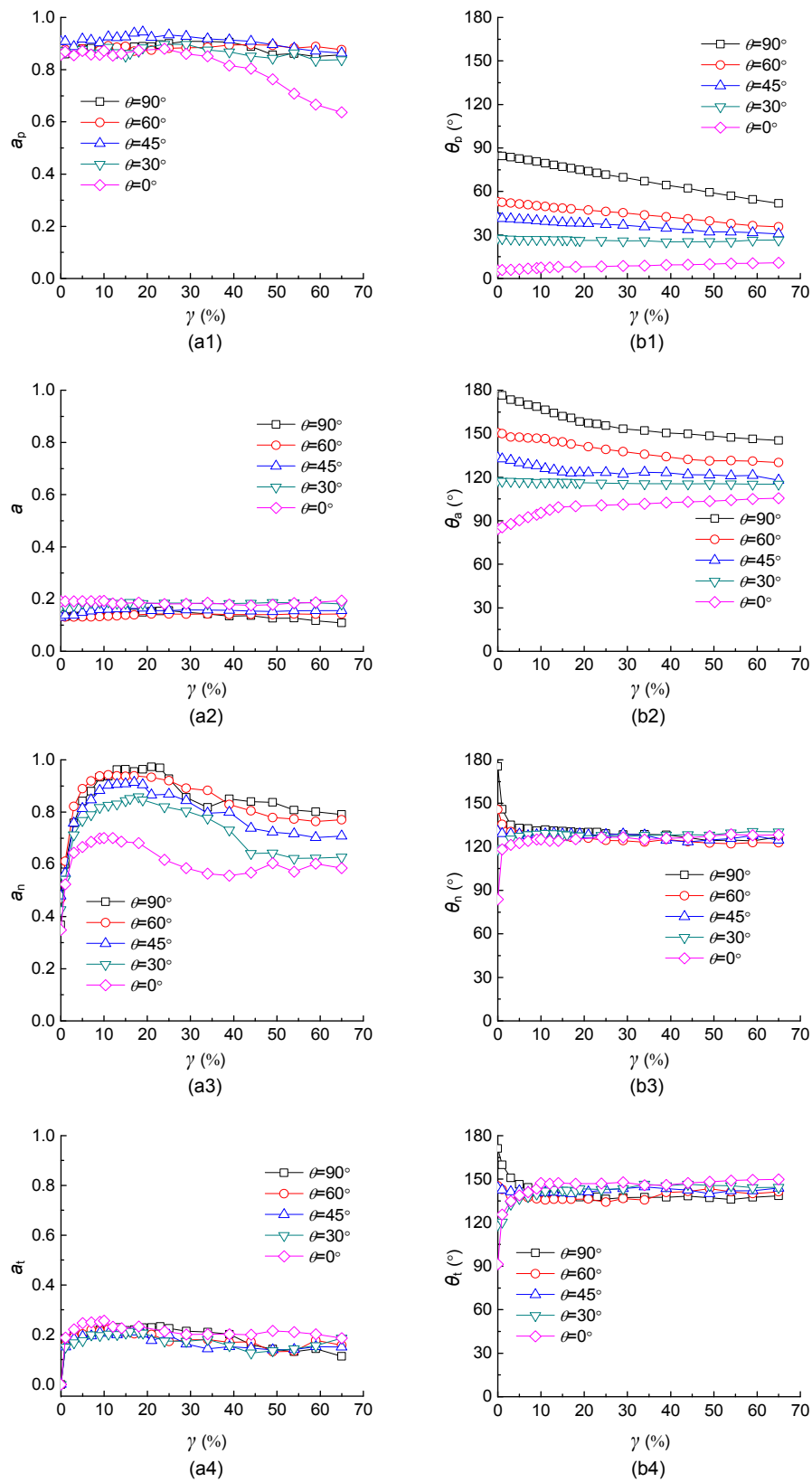
Fig. 14 Evolutions of anisotropic coefficients (a_p, a, a_n, and a_t) (a) and the principal direction angles of anisotropies (θ_p, θ_a, θ_n, and θ_t) (b) with shear strain γ of the samples with different bedding directions

5 Stress-force-fabric relationship

Stress-force-fabric relationship is an important topic in the studies of micro mechanics of granular materials (Oda, 1972; Li and Yu, 2013). Rothenburg and Bathurst (1989; 1992) presented a simple stress-force-fabric relationship based on simulated biaxial tests using both circular and oval particles:

$$\sin\phi_{ps} = \frac{1}{2}(a + a_n + a_t), \qquad (12)$$

where $\sin\phi_{ps}$ is the mobilized shear strength of the sample under the plain strain condition. The anisotropy of the initial fabric was not considered in the model. Seyedi Hosseininia (2013) proposed a new stress-force-fabric relationship to reflect the initially anisotropic fabric, but the application was limited to the biaxial shear condition, while the rotation of principal stress direction under simple shear was not considered in his study. In this study, a novel stress-force-fabric relationship incorporating the particle orientation factor will be proposed based on the simulated simple shear tests.

According to Shi *et al*. (2015), the relationship between the mobilized shear friction angle ϕ_{ps} and the simple shear friction angle ϕ_{ss} can be described as

$$\sin\phi_{ps} = \frac{\tan\phi_{ss}}{\tan\phi_{ss}\sin(\psi - 2\Delta) + \cos(\psi - 2\Delta)}, \qquad (13)$$

where ψ is the dilation angle, and Δ is the non-coaxiality angle.

As discussed earlier, the curves of principal direction of particle orientation θ_p with shear strain of samples with different bedding angles are almost symmetric to the curve of $\theta = 45°$. To consider the effect of particle orientation, a modified stress-force-fabric equation based on the form of Eq. (12) can be empirically introduced as

$$\sin\phi_{ps} = \frac{1}{2}(a + a_n + a_t) + (1 - a_p)\sin(\theta_p - \theta_p^{45°}), \quad (14)$$

where $\theta_p^{45°}$ is the principal direction of particle orientation of the $\theta = 45°$ sample.

Fig. 15 compares the computed results of $\sin\phi_{ps}$ using Eqs. (12)–(14) on DEM samples with different bedding angles. It is seen from Fig. 15 that, except for the case of $\theta = 45°$, the calculated values of $\sin\phi_{ps}$ given by Eq. (12) overestimate the simulated shear strength achieved using Eq. (13) for the cases of $\theta = 0°$ and 30°, while they underestimate the simulated strength for the cases of $\theta = 60°$ and 90°. When Eq. (14) is adopted, the above differences have been reduced, and the calculated values of $\sin\phi_{ps}$ using the new stress-force-fabric equation (Eq. (14)) are very close to the achieved shear strength using Eq. (13) for all the tested cases. Taking the $\theta = 0°$ sample for example, the maximum deviation decreases from 50% to 15% when comparing the results from Eq. (14) and Eq. (12). These results indicate that the proposed equation (Eq. (14)) well reflects the stress-force-fabric relationship of samples with initially different bedding angles. Note that Eq. (14) is an empirical equation based on a limited number of numerical simulations. Further validation is recommended before the application of the equation.

6 Conclusions

This paper studied the effect of bedding plane orientation on the simple shear behavior of dense granular assemblies using oval clumped particles in PFC2D. The effect of bedding angle on the macroscopic responses of DEM samples to simple shear, especially on non-coaxiality between the directions of the principal stress and the principal strain increment has been extensively examined. The fabric evolution of samples with different bedding angles was microscopically investigated and the influence of bedding angle was discussed. A modified stress-force-fabric relationship was proposed to quantitatively consider the bedding plane effect. Based on the simulations carried out in the study, it was found that:

1. Bedding angle has significant influence on the strength and dilatancy responses of DEM samples under simple shear. The peak friction angle and peak dilation angle of DEM samples both increase with bedding angle, and the numerical simulations are in good agreement with the historical experimental results on real sands. The peak friction angle of DEM
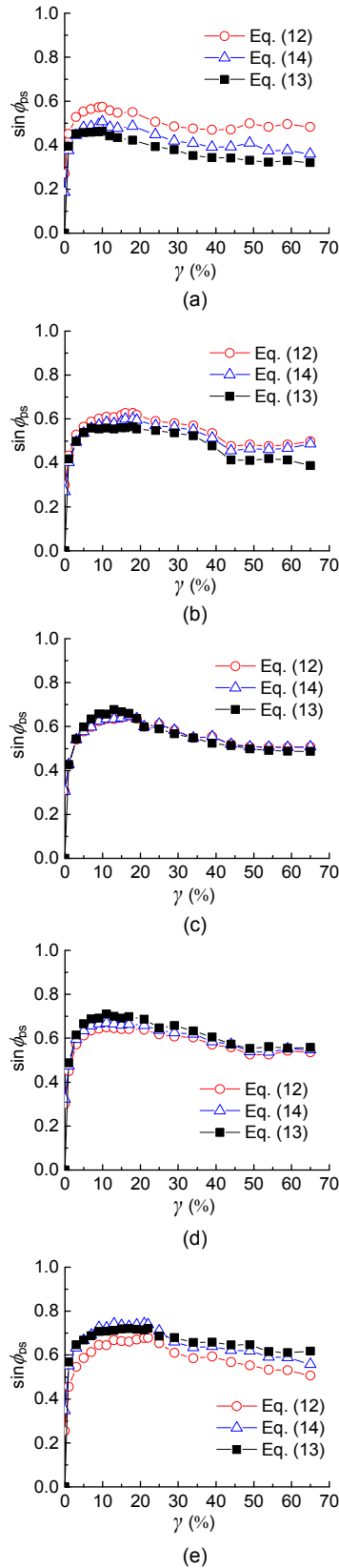
Fig. 15 Validation of the stress-force-fabric relationship
(a) θ=0°; (b) θ=30°; (c) θ=45°; (d) θ=60°; (e) θ=90°

sample can increase to about 16° when the bedding angle increases from 0° to 90°, and this behavior is quite comparable to the physical biaxial test results using 2D oval photoelastic rods as published in the literature.

2. The non-coaxility is affected by bedding angle. Considerable difference in the non-coaxility angle can be observed within the shear strain range of $\gamma \leq 40\%$, and the larger the bedding angle, the greater the non-coaxiality. The proposed stress-dilatancy equation (Eq. (10)) can well describe the non-coaxial stress-dilatancy behavior of DEM samples under simple shear, independent of particle shape and initial fabric.

3. The anisotropic coefficients of particle orientation and contact normal are not very sensitive to bedding angle and do not change much with shear strain. For samples with different bedding angles, the major directions of particle orientation have a tendency to approach the directions of major principal stress plane under simple shear loading. During shear, the major directions of contact normal are all nearly normal to principal directions of particle orientation, irrespective of the variation of bedding angle.

4. The effect of bedding angle on the distribution of contact forces is dominantly dependent on the evolution of normal contact force anisotropy, whilst the extent of tangential contact force anisotropy is minimal and little affected by bedding angle. The inclinations of major directions of contact forces are strongly affected by the rotation of the principal stress, the directions of normal and tangential contact forces converge quickly at lower shear strain levels, i.e., $\gamma \leq 10\%$, and directions in the residual state are not much affected by the bedding directions of particles.

5. Compared with Rothenburg and Bathurst's equation (Eq. (12)), the proposed stress-force-fabric relationship (Eq. (14)) incorporating the anisotropic parameters of particle orientation can well predict the shear strength of samples with initially different bedding angles. The maximum deviation between the predicted and the simulated mobilized shear strength can decrease from 50% to 15% when the new relationship (Eq. (14)) is applied.

References

Alshibli, K.A., Sture, S., Costes, N.C., *et al*., 2000. Assessment of localized deformations in sand using X-ray computed

tomography. *Geotechnical Testing Journal*, **23**(3):274-299.
http://dx.doi.org/10.1520/GTJ11051J

Arthur, J.R.F., Menzies, B.K., 1972. Inherent anisotropy in a sand. *Géotechnique*, **22**(1):115-128.
http://dx.doi.org/10.1680/geot.1972.22.1.115

Brewer, R., 1964. Fabric and Mineral Analysis of Soils. John Wiley & Sons, Ltd., USA.
http://dx.doi.org/10.1097/00010694-196507000-00024

Cavarretta, I., Coop, M., O'Sullivan, C., 2010. The influence of particle characteristics on the behavior of coarse grained soils. *Géotechnique*, **60**(6):413-424.
http://dx.doi.org/10.1680/geot.2010.60.6.413

Chen, L.P., Zhang, D.L., Fang, Q., *et al*., 2014. Research on friction characteristics and failure mechanism of anisotropic sand based on micro-statistics. *Chinese Journal of Rock Mechanics and Engineering*, **33**(S1):3291-3298 (in Chinese).

Drescher, A., de Jong, G.D.J., 1972. Photoelastic verification of a mechanical model for the flow of a granular material. *Journal of the Mechanics and Physics of Solids*, **20**(5): 337-340.
http://dx.doi.org/10.1016/0022-5096(72)90029-4

Guo, P.J., 2008. Modified direct shear test for anisotropic strength of sand. *Journal of Geotechnical and Geoenvironmental Engineering*, **134**(9):1311-1318.
http://dx.doi.org/10.1061/(ASCE)1090-0241(2008)134:9 (1311)

Hu, M.Y., O'Sullivan, C., Jardine, R.R., *et al*., 2010. Stress-induced anisotropy in sand under cyclic loading. *Granular Matter*, **12**(5):469-476.
http://dx.doi.org/10.1007/s10035-010-0206-7

Itasca, 2008. Two Dimensional Particle Flow Code: Software Manual (Version 4.0). Itasca Consulting Group, Inc., Minneapolis, USA.

Jiang, M.J., Sun, C., Crosta, G.B., *et al*., 2015. A study of submarine steep slope failures triggered by thermal dissociation of methane hydrates using a coupled CFD-DEM approach. *Engineering Geology*, **190**:1-16.
http://dx.doi.org/10.1016/j.enggeo.2015.02.007

Konishi, J., Oda, M., Nemat-Nasser, S., 1983. Induced anisotropy in assemblies of oval cross-sectional rods in biaxial compression. *In*: Jenkins, J.T., Satake, M. (Eds.), Mechanics of Granular Material: New Models and Constitutive Relations. Elsevier Science Publishers, the Netherlands, p.31-39.
http://dx.doi.org/10.1016/B978-0-444-42192-0.50010-4

Lai, H.J., Zheng, J.J., Zhang, R.J., *et al.*, 2016. Visualization of the formation and features of soil arching within a piled embankment by discrete element method simulation. *Journal of Zhejiang University-SCIENCE A (Applied Physics & Engineering)*, **17**(10):803-817.
http://dx.doi.org/10.1631/jzus.A1500302

Li, X., Yu, H.S., 2013. On the stress-force-fabric relationship for granular materials. *International Journal of Solids and Structures*, **50**(9):1285-1302.
http://dx.doi.org/10.1016/j.ijsolstr.2012.12.023

Mahmood, I., Iwashita, K., 2010. Influence of inherent anisotropy on mechanical behavior of granular materials based on DEM simulations. *International Journal for Numerical and Analytical Methods in Geomechanics*, **34**(8):795-819.
http://dx.doi.org/10.1002/nag.830

Miura, K., Miura, S., Toki, S., 1986. Deformation behavior of anisotropic dense sand under principal stress axes rotation. *Soils and Foundations*, **26**(1):36-52.
http://dx.doi.org/10.3208/sandf1972.26.36

Munjiza, A., 2004. The Combined Finite-discrete Element Methods. John Wiley & Sons, Ltd., USA.
http://dx.doi.org/10.1002/0470020180

Ng, T.T., Aube, D., Altobelli, S., 2002. Void distribution of sand specimens by MRI. 15th ASCE Engineering Mechanics Conference, p.1-7.

Oda, M., 1972. Initial fabrics and their relations to mechanical properties of granular material. *Soils and Foundations*, **12**(1):17-36.
http://dx.doi.org/10.3208/sandf1960.12.17

Oda, M., Konishi, J., 1974. Rotation of principal stresses in granular material during simple shear. *Soils and Foundations*, **14**(4):39-53.
http://dx.doi.org/10.3208/sandf1972.14.4_39

Oda, M., Nakayama, H., 1989. Yield function for soil with anisotropic fabric. *Journal of Engineering Mechanics*, **115**(1):89-104.
http://dx.doi.org/10.1061/(asce)0733-9399(1989)115:1(89)

Oda, M., Konishi, J., Nemat-Nasser, S., 1982. Experimental micromechanical evaluation of strength of granular materials: effects of particle rolling. *Mechanics of Materials*, **1**(4):269-283.
http://dx.doi.org/10.1016/0167-6636(82)90027-8

Oda, M., Nemat-Nasser, S., Konishi, J., 1985. Stress-induced anisotropy in granular masses. *Soils and Foundations*, **25**(3):85-97.
http://dx.doi.org/10.3208/sandf1972.25.3_85

O'Sullivan, C., 2011. Particulate Discrete Element Modeling: a Geomechanics Perspective. Taylor and Francis, UK.

Pradhan, T.B.S., Tatsuoka, F., Horii, N., 1988. Simple shear testing on sand in a torsional shear apparatus. *Soils and Foundations*, **28**(2):95-112.
http://dx.doi.org/10.3208/sandf1972.28.2_95

Procter, D.C., Barton, R.R., 1974. Measurement of the angle of interparticle friction. *Géotechnique*, **24**(4):581-604.
http://dx.doi.org/10.1680/geot.1974.24.4.581

Qian, J.G., You, Z.P., Huang, M.S., 2013. Anisotropic characteristics of granular materials under simple shear. *Journal of Central South University*, **20**(8):2275-2284.
http://dx.doi.org/10.1007/s11771-013-1734-1

Rothenburg, L., Bathurst, R.J., 1989. Analytical study of induced anisotropy in idealized granular materials. *Géotechnique*, **39**(4):601-614.
http://dx.doi.org/10.1680/geot.1989.39.4.601

Rothenburg, L., Bathurst, R.J., 1992. Micromechanical features of granular assemblies with planar elliptical particles. *Géotechnique*, **42**(1):79-95.

http://dx.doi.org/10.1680/geot.1992.42.1.79

Satake, M., 1978. Constitution of mechanics of granular materials through graph representation. Proceedings of the 26th Japan National Congress on Theoretical and Applied Mechanics, p.257-266.

Seyedi Hosseininia, E., 2013. Stress-force-fabric relationship for planar granular materials. *Géotechnique*, **63**(10):830-841.
http://dx.doi.org/10.1680/geot.12.P.055

Shen, C.K., O'Sullivan, C., Jardine, R.J., 2011. A micromechanical investigation of drained simple shear tests. International Symposium on Deformation Characteristics of Geomaterials, p.314-321.

Shi, D.D., Xue, J.F., Zhao, Z.Y., *et al.*, 2015. A DEM investigation on simple shear behavior of dense granular assemblies. *Journal of Central South University*, **22**(12): 4844-4855.
http://dx.doi.org/10.1007/s11771-015-3036-2

Shi, D.D., Zheng, L., Xue, J.F., *et al.*, 2016. DEM modeling of particle breakage in silica sands under one-dimensional compression. *Acta Mechanica Solida Sinica*, **29**(1):78-94.
http://dx.doi.org/10.1016/S0894-9166(16)60008-3

Shibuya, S., Mitachi, T., Tamate, S., 1997. Interpretation of direct shear box testing of sands as quasi-simple shear. *Géotechnique*, **47**(4):769-790.
http://dx.doi.org/10.1680/geot.1997.47.4.769

Thay, S., Likitlersuang, S., Pipatpongsa, T., 2013. Monotonic and cyclic behavior of Chiang Mai sand under simple shear mode. *Geotechnical and Geological Engineering*, **31**(1):67-82.
http://dx.doi.org/10.1007/s10706-012-9563-9

Thomas, P.A., Bray, J.D., 1999. Capturing nonspherical shape of granular media with disk clusters. *Journal of Geotechnical and Geoenvironmental Engineering*, **125**(3): 169-178.
http://dx.doi.org/10.1061/(asce)1090-0241(1999)125:3(169)

Thornton, C., 2000. Numerical simulations of deviatoric shear deformation of granular media. *Géotechnique*, **50**(1):43-53.
http://dx.doi.org/10.1680/geot.2000.50.1.43

Thornton, C., Zhang, L., 2006. A numerical examination of shear banding and simple shear non-coaxial flow rules. *Philosophical Magazine*, **86**(21-22):3425-3452.
http://dx.doi.org/10.1080/14786430500197868

Ting, J.M., Meachum, L.R., 1995. Effect of bedding plane orientation on the behavior of granular systems. Joint Applied Mechanics and Materials Summer Meeting, p.43-57.

Tong, Z.X., Fu, P.C., Zhou, S.P., *et al.*, 2014. Experimental investigation of shear strength of sands with inherent fabric anisotropy. *Acta Geotechnica*, **9**(2):257-275.
http://dx.doi.org/10.1007/s11440-014-0303-6

Wang, J., Dove, J.E., Gutierrez, M.S., 2007. Discrete-continuum analysis of shear banding in the direct shear test. *Géotechnique*, **57**(6):513-526.
http://dx.doi.org/10.1680/geot.2007.57.6.513

Yan, W.M., Zhang, L., 2013. Fabric and the critical state of

idealized granular assemblages subject to biaxial shear. *Computers and Geotechnics*, **49**:43-52.
http://dx.doi.org/10.1016/j.compgeo.2012.10.015

Yang, Z.X., Yang, J., Wang, L.Z., 2012. On the influence of inter-particle friction and dilatancy in granular material: a numerical analysis. *Granular Matter*, **14**(3):433-447.
http://dx.doi.org/10.1007/s10035-012-0348-x

Yang, Z.X., Yang, J., Wang, L.Z., 2013. Micro-scale modeling of anisotropy effects on undrained behavior of granular soils. *Granular Matter*, **15**(5):557-572.
http://dx.doi.org/10.1007/s10035-013-0429-5

Zhou, J., Shi, D.D., Jia, M.C., 2007. Numerical simulation of mechanical response on sand under monotonic loading by particle flow code. *Journal of Tongji University*, **35**(10): 1299-1304 (in Chinese).

中文概要

题　目：椭圆颗粒层理面定向对密实颗粒试样单剪力学特性的影响

目　的：利用离散元数值模拟技术，从宏细观角度探究单剪受荷模式下，颗粒定向引起的层理面效应对数值试样强度与变形特征、应力-剪胀关系以及组构各向异性演化的影响及其机理。

创新点：1. 分析了单剪受荷条件下应力主轴偏转引发的主应力与主应变增量之间的非共轴效应，针对密实颗粒试样，研究了初始层理面倾角对非共轴应力-剪胀关系的影响；2. 从细观力学角度，研究了应力主轴偏转条件下初始不同层理面试样的应力诱发组构各向异性特征，提出了一个可以考虑初始层理面效应的应力-接触力-组构经验关系式。

方　法：1. 采用离散元团聚颗粒方法构建初始不同层理面定向的数值试样；2. 采用傅里叶级数近似法对数值试样细观组构各向异性演化规律进行统计和定量数学分析；3. 通过与已有文献数值模拟和室内试验结果的对比，探讨密实颗粒数值试样的单剪特性及非共轴应力-剪胀关系。

结　论：1. 初始层理面定向显著影响数值试样的单剪强度与体变特征，且在定量上能与室内物理试验结果进行对比；2. 在单剪受荷模式下，初始层理角越大，非共轴效应越显著；3. 随着应力主轴的偏转，颗粒定向各向异性主方向逐渐趋于大主应力面作用方向，而接触法向各向异性的主方向基本垂直于颗粒定向各向异性主方向。4. 本文提出的应力-接触力-组构关系式能够较好的反映颗粒定向对试样抗剪强度的影响。

关键词：初始组构各向异性；颗粒定向；单剪；非共轴；离散单元法